



CHORUS

This is the accepted manuscript made available via CHORUS. The article has been published as:

Atomic-resolution visualization and doping effects of complex structures in intercalated bilayer graphene

Jason P. Bonacum, Andrew O'Hara, De-Liang Bao, Oleg S. Ovchinnikov, Yan-Fang Zhang, Georgy Gordeev, Sonakshi Arora, Stephanie Reich, Juan-Carlos Idrobo, Richard F.

Haglund, Sokrates T. Pantelides, and Kirill I. Bolotin

Phys. Rev. Materials **3**, 064004 — Published 28 June 2019

DOI: [10.1103/PhysRevMaterials.3.064004](https://doi.org/10.1103/PhysRevMaterials.3.064004)

Atomic-Resolution Visualization and Doping Effects of Complex Structures in Intercalated Bilayer Graphene

Jason P. Bonacum¹, Andrew O'Hara¹, De-Liang Bao^{1,2}, Oleg S. Ovchinnikov^{1,3}, Yan-Fang Zhang¹, Georgy Gordeev⁴, Sonakshi Arora⁴, Stephanie Reich⁴, Juan-Carlos Idrobo⁵, Richard F. Haglund¹, Sokrates T. Pantelides^{1,5,6}, Kirill Bolotin^{1,4}

¹*Department of Physics and Astronomy, Vanderbilt University, Nashville, TN, USA*

²*Institute of Physics and University of Chinese Academy of Sciences, Chinese Academy of Sciences, Beijing 100190, China*

³*Institute for Functional Imaging of Materials, Oak Ridge National Laboratory, Oak Ridge, TN, USA*

⁴*Freie Universität Berlin, Fachbereich Physik, Institut für Experimentalphysik, Arnimallee 14, 14195 Berlin, Germany*

⁵*Center for Nanophase Materials Sciences, Oak Ridge National Laboratory, Oak Ridge, TN, USA*

⁶*Department of Electrical Engineering and Computer Science, Vanderbilt University, Nashville, TN 37235, USA*

Molecules intercalating two-dimensional (2D) materials form complex structures that have been mostly characterized by spatially averaged techniques. Here we use aberration-corrected scanning transmission electron microscopy and density-functional-theory (DFT) calculations to study the atomic structure of bilayer graphene (BLG) and few-layer graphene (FLG) intercalated with FeCl₃. In BLG we discover two distinct intercalated structures that we identify as monolayer-FeCl₃ and monolayer-FeCl₂. The two structures are separated by atomically sharp boundaries and induce large free-carrier densities of order 10¹³ cm⁻² in the graphene layers. In FLG, we observe multiple FeCl₃ layers stacked in a variety of possible configurations with respect to one another. Finally, we find that the microscope's electron beam can convert the FeCl₃ monolayer into FeOCl monolayers in a rectangular lattice. These results reveal the need for a combination of atomically-resolved microscopy, spectroscopy, and DFT calculations to identify intercalated structures and study their properties.

This manuscript has been authored by UT-Battelle, LLC under Contract No. DE-AC05-00OR22725 with the U.S. Department of Energy. The United States Government retains and the publisher, by accepting the article for publication, acknowledges that the United States Government retains a non-exclusive, paid-up, irrevocable, worldwide license to publish or reproduce the published form of this manuscript, or allow others to do so, for United States Government purposes. The Department of Energy will provide public access to these results of federally sponsored research in accordance with the DOE Public Access Plan (<http://energy.gov/downloads/doe-public-access-plan>).

I. INTRODUCTION

Graphite intercalation compounds (GICs), assemblies of foreign atoms or molecules in the van der Waals gaps between the carbon layers, have been studied for over a century for potential applications in energy storage, high-temperature superconductivity, and reaction catalysis [1–5]. The recent ability to isolate graphite with controlled number of carbon layers led to a surge of interest in intercalated few-layer graphene (FLG) and bilayer graphene (BLG) by either single atomic species, e.g. Li or Na, or molecules [6–10]. Few-layer graphene intercalated with iron chloride (FLG-FeCl₃) is a particularly interesting example of such a compound, although FeCl₃-intercalated BLG (BLG-FeCl₃) has received limited attention [11]. Experiments have found that the presence of FeCl₃ causes decoupling of the carbon layers, resulting in a graphene-like band structure and induces a very large carrier density up to 10^{14} cm⁻² in the graphene sheets (corresponding to a Fermi level shift as large as 1.3 eV below the Dirac point) [12]. Highly doped graphene and intercalated graphite are interesting for the study of exotic superconductivity [13,14]. In addition, it has been suggested that FLG-FeCl₃ develops an interesting magnetic structure with ferromagnetic order inside each FeCl₃ layer and antiferromagnetic coupling between the neighboring layers [15]. Such order is especially interesting in the context of the recent interest in two-dimensional magnetism [16–20]. Finally, FLG-FeCl₃ is stable in the ambient conditions over months, resists to degradation by common solvents, and has both high conductivity and high optical transparency [11,12]. These properties invite potential applications for energy storage, transparent conductors, and heat spreaders [21,22].

At the same time, while multiple experiments addressed the macroscopic properties of FLG-FeCl₃, its microscopic structure remains virtually unknown and the possibility that multiple intercalant structures form has not been adequately explored. Electron diffraction and

powder X-ray diffraction (XRD) data from FeCl₃-GICs suggest that within each van der Waals gap the FeCl₃ molecules form a honeycomb lattice similar to bulk FeCl₃ [2,23]. XRD, however, being a spatially averaged technique, is not sensitive to several possibilities. For example, intercalant layers in FLG may have layer-number dependent properties, as is known to occur in the lithium intercalation process [24]. Such properties should be studied to understand the predicted antiferromagnetic coupling between neighboring FeCl₃ layers [15]. Previous research also demonstrates that FeCl₃ is converted to FeCl₂ in a reducing environment, but the published work on the stability of FLG-FeCl₃ does not consider the possibility of FeCl₂ formation [2]. Lattice defects in FLG-FeCl₃, if present, have not so far been investigated by any means, but are expected to strongly scatter the charge carriers in graphene layers, thereby limiting applicability of FLG-FeCl₃ in electronics. The presence of defects should also affect the dynamics of the intercalation process and thus be critical for energy storage applications.

In this paper, we report atomic-resolution structures of FLG and BLG intercalated with FeCl₃. Aberration-corrected scanning transmission electron microscopy (STEM) of BLG-FeCl₃ reveals two distinct structures that, in combination with density-functional-theory (DFT) calculations and STEM image simulations, are identified as monolayer-FeCl₃ and monolayer-FeCl₂. Both structures exhibit a hexagonal crystal structure, sharp boundaries between intercalated and unintercalated regions, and lattice defects. The presence of two structures and their effects on doping are confirmed via electron energy loss spectroscopy (EELS) and Raman spectroscopy and discussed in the context of DFT calculations. We also observe a rectangular lattice of FeOCl that is formed at the edges of the FeCl₃ monolayer when exposed to the electron beam during STEM imaging. In FeCl₃-intercalated FLG, we observe stacked FeCl₃ monolayers that display no preferred orientation of the FeCl₃ from layer to layer. Our results shed light on the origin of

doping in intercalated graphene, its stability, and may help in understanding magnetic properties of intercalated systems.

The samples were fabricated using the vapor transport method of intercalation [2,12]. Bilayer graphene and few-layer graphene were transferred onto holes (2 μm diameter) in silicon nitride membranes, as seen in the top right panel of Fig. 1. The samples were vacuum sealed in borosilicate ampules with anhydrous FeCl_3 and then transferred to a tube furnace for the intercalation reaction. After intercalation, the samples were washed with deionized water to remove any adsorbed FeCl_3 that could interfere with imaging of the intercalated FeCl_3 . Raman spectroscopy was performed before and after intercalation to confirm the presence of FeCl_3 , which is evidenced by new blue-shifted G peaks [12]. Additional experimental details are provided in the Methods section and in the Supplemental Material.

II. ATOMIC STRUCTURE OF FeCl_3 MONOLAYER

Aberration-corrected STEM was used to investigate the atomic structure of the resulting intercalants. Atomic-resolution images were obtained using an annular dark field (ADF) detector, and the elemental composition was confirmed using EELS, as illustrated in Fig. 1, where we show data for a FeCl_3 -BLG sample. While intercalated iron and chlorine are clearly resolved, carbon atoms are barely visible as the ADF signal strength is roughly proportional to the square of the atomic number. Thus, the Fe and Cl signals are roughly nineteen and eight times stronger, respectively, than the carbon signals. A key result of this investigation is that we were able to identify both FeCl_3 and FeCl_2 in adjacent regions, which indicates that FeCl_3 molecules can undergo reduction within the van der Waals gap of BLG. We first present the data and analysis for FeCl_3 intercalants. The pertinent ADF image [Fig. 2(a)] exhibits a 2D honeycomb structure. This structure is the same as in bulk FeCl_3 with each

iron atom bonded to six chlorine atoms in an octahedral geometry, as shown in Fig. 2(b). The carbon atoms can be seen faintly inside the holes of the FeCl_3 honeycomb lattice displayed in Fig. 2(a), although the contrast is much lower than that of the chlorine and iron atoms. In areas where there is incomplete intercalation [Fig. 2(d)], the intercalants form islands that are separated from neighboring unintercalated regions by an atomically sharp boundary. This sharpness is due to in-plane covalent bonds between the iron chloride molecules in the intercalant layer.

To unambiguously determine the position of each atomic species with STEM simulations, atomic positions optimized by DFT calculations and the experimental beam parameters were used as inputs to the QSTEM software package to create simulated ADF images [Fig. 2(c)] for comparison to the experimentally obtained images [25]. There is good agreement between the ADF image and STEM simulation. The measured FeCl_3 lattice constant of 0.61 ± 0.01 nm agrees with the theoretical value of 0.60 nm. These data demonstrate that the intercalated FeCl_3 forms a 2D material in between the graphene layers. [The \$\text{FeCl}_3\$ monolayer is stable against air and water exposure when encapsulated in the BLG, which is also corroborated by previous studies that show the stability of \$\text{FeCl}_3\$ -intercalated FLG \[11,12\]. To our knowledge, free standing monolayer \$\text{FeCl}_3\$ has not been realized because it is an oxidizing agent and readily forms hydrates in the presence of moisture.](#)

In order to better resolve carbon atoms and reduce surface contamination effects, we filtered the original data [Fig. 2(e)] using principal component analysis (PCA) [26,27]. We noticed that the first PCA component corresponds primarily to the surface contamination and the higher order components (>10) correspond to background noise in the image. We therefore plotted the components 2 through 10 [Fig. 2(f)]. The three types of atoms present in the samples are visible in the images. While the background is dark blue, iron atoms appear yellow, chlorine atoms – green, and carbon atoms – light blue.

These light blue spots are separated by 0.57 ± 0.01 nm, which corresponds to four times the carbon-carbon bond in graphene, and sometimes appear off center or as dumbbells inside the hexagons of the FeCl_3 lattice. These observations further confirm the source of the light blue spots as the carbon lattice and not an artifact from the FeCl_3 structure, which would have similar hexagonal symmetry. The location of the carbon atoms indicates that the carbon lattice and FeCl_3 lattice are aligned with each other in this sample. The PCA filtering also displays interstitial iron atoms in the FeCl_3 hexagons. While interstitial iron can be seen on the left-center edge of the unfiltered image [Fig. 2(e)], the removal of the surface contamination in the image makes it clear that several such interstitials occur in this section of the sample. Such additional interstitial iron atoms at non-regular lattice sites are likely to impact the magnetic ordering properties of FeCl_3 -intercalated FLG [15].

III. ATOMIC STRUCTURE OF FeCl_2 MONOLAYER

We now turn to the region of the intercalant structure that is different from the honeycomb structure described above, which we identify as FeCl_2 . The pertinent ADF image is shown in Fig. 3(a). The structure in Fig. 3(a) looks similar to a monolayer of FeCl_3 , but with an additional iron atom in the holes of the honeycomb lattice, signifying a change in stoichiometry from FeCl_3 to FeCl_2 . Comparison of this structure to a STEM simulation of monolayer FeCl_2 [Fig. 3(b)] exhibits good agreement, with an experimental lattice parameter of 0.350 ± 0.005 nm compared to the theoretical value of 0.347 nm. We further probed the same region by EELS, which is sensitive to the iron oxidation state. We focus on spectral features corresponding to iron core electron excitations, highlighted yellow in Fig. 1. These features include a step-like edge and Lorentzian-shaped peaks, referred to as white-lines [Fig. 3(c)]. The ratio of the L_3 and L_2 white-line intensities is used to differentiate between Fe^{2+}

and Fe^{3+} species, which have L_3/L_2 intensity ratios of 4.0 and 5.5 respectively [28]. Experimentally, we determined that ratio using both Lorentzian fits as well the analysis of the second derivative of the data (see Supplemental Material for more details) [28]. Both methods yield the ratio of 4 ± 1 , consistent with the structure being FeCl_2 . We suggest that FeCl_3 is partially reduced to FeCl_2 during the process of intercalating FeCl_3 . This happens due to the presence of a reducing agent, which could be hydrocarbon contaminants or hydrogen that outgases from the walls of the borosilicate reaction vessel.

IV. DOPING EFFECTS OF FeCl_3 AND FeCl_2

A. Raman spectroscopy

We find further evidence for the coexistence of FeCl_3 and FeCl_2 regions in FeCl_3 -BLG in their effects on the free carrier density of graphene. The carrier density in graphene, as well as its proxy, the position of the Fermi energy relative to the Dirac point, were probed via Raman spectroscopy. Before intercalation, the Raman G mode peak is at 1582 cm^{-1} . After intercalation, the G peak splits into three peaks – G0, G1, and G2 at 1586 cm^{-1} , 1614 cm^{-1} , and 1626 cm^{-1} respectively [Fig. 4(a)]. Since the spectral position of the G mode is indicative of the local free carrier density of graphene, such splitting is consistent with the presence of regions with three distinct carrier densities within the diffraction-limited laser spot on the sample [29,30]. With its spectral position within 4 cm^{-1} from the G peak before intercalation, the G0 peak indicates undoped graphene, while G1 and G2 correspond to higher carrier densities. The slight shift of the G0 peak after intercalation is likely due to the addition of surface contamination during the intercalation process, as seen in the STEM images. To determine these carrier densities quantitatively, we varied the laser excitation energy. The peaks G1 and G2 exhibit maximum intensities at 1.96 eV and 2.07 eV excitation energies respectively,

while the G0 peak intensity is relatively constant with excitation energy [Fig. 4(b)]. The maximum in G peak intensity at a certain excitation energy signals that the local Fermi energy is half the excitation energy [31]. Assuming that FeCl₃ is an acceptor molecule, we therefore determine that the Fermi energy corresponding to G0 is at the local Dirac point, while those for G1 and G2 are 0.98 eV and 1.03 eV below the local Dirac point, respectively, as illustrated in Fig. 4(c). The number of free carriers in each region can be approximated via the relation $n \approx \frac{1}{\pi}(E_F/v_F\hbar)^2$. We determine the carrier densities of ~ 0 cm⁻², 7.1×10^{13} cm⁻² and 7.8×10^{13} cm⁻² for G0, G1, and G2 respectively.

B. Discussion

Combining the Raman spectroscopy results with the STEM data, we draw several conclusions about the atomic origin of the different free carrier densities. In the literature, the appearance of two blue-shifted G peaks is attributed to staging or surface adsorption of FeCl₃ [12,32]. However, staging does not occur in BLG. In our STEM images, there is only a single monolayer of FeCl₃ between the layers of graphene and no adsorbed FeCl₃ on its surface. The presence of both the G1 and G2 peaks therefore evinces the presence of two different types of intercalants that locally induce different doping levels. We hypothesize that the coexistence of FeCl₃ and FeCl₂, as portrayed in Fig. 4(c), is responsible for the two positions of the universal Fermi energy relative to the local Dirac points. This hypothesis is supported by DFT calculations that exhibit two different positions for the Fermi level below the Dirac point, 0.42 eV for FeCl₂ and 0.66 eV for FeCl₃. The smaller theoretical values of the Fermi energy relative to the local Dirac point compared to the experimental values is likely due to the underestimation of the Fermi velocity within the local density approximation [33]. [The difference of the hole doping densities in FeCl₃-BLG and FeCl₂-BLG is small, but its presence is corroborated by DFT results, which find an even](#)

[larger difference \(0.24 eV as opposed to 0.05 eV\). A possible non-uniformity in contaminants or strain may influence the measured difference.](#)

The appearance of free carriers in graphene layers adjacent to another material is typically interpreted as charge transfer. We used the present DFT-calculated charge densities in the intercalated BLG to test this interpretation. We found that, while the Fermi energy deviates from the Dirac point in FeCl₃-BLG, there is virtually no net charge transfer between the graphene and intercalant layers. Although the drop of the Fermi level below the Dirac point suggests a net transfer of electrons from the graphene to the intercalant, the wavefunctions from the valence states in the FeCl₃ extend into the graphene layers thereby maintaining overall charge neutrality. In other words, the proximity of graphene to another material causes a redistribution of electrons in the *energy space* to produce free carriers (doping), seemingly corresponding to charge transfer, the distribution of electrons in physical space actually remains relatively unchanged (see Supplemental Material for details).

The DFT results also demonstrate that the individual graphene layers in BLG do not in fact decouple after intercalation to form band structures like that of monolayer graphene. This feature is different from what has been inferred by Raman spectroscopy on FeCl₃-intercalated FLG and calculations for stage-1 FeCl₃-intercalated bulk graphite, probably due to the multilayer structure of the latter two systems [12,34]. When AB-stacked BLG is intercalated with FeCl₃, the band structure resembles that of AA-stacked BLG but with a smaller energy scale for the band splitting. However, this finding does not affect the interpretation of the Raman spectra because the linear dispersion and Kohn anomaly are maintained at the K point (see Supplemental Material for details).

Overall, our DFT and Raman spectroscopy data suggest the association of the peaks G0, G1, and G2 with unintercalated regions, regions intercalated with FeCl₂, and regions intercalated with FeCl₃ respectively. Our STEM data are

consistent with this assignment. The presence of the G0 peak is corroborated by the observation of unintercalated regions in STEM images.

V. ALIGNMENT OF MULTIPLE FeCl₃ MONOLAYERS

A. Interpreting the alignment from atomic-resolution images

We also imaged intercalated FLG with thicknesses of four to six graphene layers to study the relative angular alignment of FeCl₃ monolayers sandwiched between successive layers of graphene and test whether a superposition of FeCl₃ and FeCl₂ layers needs to be invoked to reproduce the images. The ADF images [Fig. 5] reveal only FeCl₃ layers with different degrees of alignment for different samples. The first sample [Fig. 5(a)] exhibits complete angular alignment of the FeCl₃ layers, observed as coincident ADF signal from the atoms in each layer. The stacking configuration is inferred by comparing the ADF image with STEM simulations of bilayer and trilayer FeCl₃ and FeCl₂ in different stacking configurations. Two and three layers were used since the sample had approximately four to six layers of graphene, determined by atomic force microscopy, and the Raman spectrum of the sample after intercalation indicates partial intercalation (see Supplemental Material for more details). The best agreement between the ADF image and STEM simulation is for ABC stacking of FeCl₃ when comparing AA, AB, AAA, ABA, and ABC stacking configurations of both FeCl₃ and FeCl₂. The STEM simulation for ABC-stacked FeCl₃ is shown in Fig. 5(b), while the simulations for the other stacking configurations can be found in the Supplemental Material.

The second sample exhibits small angles of rotation between the intercalant layers, producing a moiré pattern in the ADF image [Fig. 5(c)]. The relative angles between each monolayer were determined from the fast Fourier transformation (FFT) of the ADF image. The FFT of the second

sample [Fig. 5(d)] displays sharp Fourier peaks in a hexagonal pattern due to the hexagonal structure of the crystal basis for FeCl₃. We assume only FeCl₃ is present in this section of the sample given the greater relative abundance of FeCl₃ compared FeCl₂ in the previous samples. Each layer of FeCl₃ has a distinctive set of Fourier peaks, and the relative angle between the layers can be observed from the angles between those Fourier peaks. Three distinct sets of peaks can be seen in Fig. 5(d) with angles of 0°, 3.0°, and 5.5°. Given these angles, the lattice parameter of the moiré pattern ($a_{\text{moiré}}$) can be calculated using the following equation (see Supplemental Material for further details):

$$a_{\text{moiré}} = \frac{a}{\sqrt{2(1 - \cos \theta)}} \quad (1)$$

where a is the lattice parameter of the FeCl₃ measured from the ADF image and θ is the relative angle between each layer measured from the FFT. Using the values of 3.0° and 2.5° in equation 1, the moiré lattice parameter is 12nm and 14nm respectively. The moiré patterns for these angles cannot be seen in the ADF image [Fig. 5(c)] as they are too large for the size of the image, but 5.5° gives a moiré lattice parameter of 6.3 nm, which agrees with the moiré lattice parameter, 6.2±0.1 nm, seen in Fig. 5(c).

The third sample exhibits angles between FeCl₃ layers as large as 44° measured in the FFT [Fig. 5(f)], that corresponds to $a_{\text{moiré}}$ of 0.81 nm, close to the lattice parameter of FeCl₃ (0.607 nm). There are also at least six distinct Fourier peaks spread across the 44° creating an FFT that resembles that of a polycrystal. The ADF image for this sample [Fig. 5(e)] appears disordered due to the number of layers and wide range of angles, but faint moiré patterns can still be seen from the layers of FeCl₃ that have small relative angles to each other, which correspond to moiré-pattern lattice parameters on the order of nanometers.

B. Explaining the results with DFT calculations

To gain insight into the source of the observed moiré patterns and apparent polycrystalline structure, we calculated the interlayer cohesion energetics as a function of twist angle between FeCl_3 and graphene, as shown in Fig. 4(g). For the calculated angles, we find that there is a global energy minimum at $0^\circ/60^\circ$ and additional local energy minima at 10° , 25° , 35° , and 50° . However, the overall range of energies is only 65 meV per FeCl_3 unit. That energy range is significantly smaller than the available thermal energy ($\sim 6kT = 300$ meV per FeCl_3 unit) suggesting that patches can nucleate with essentially any relative angle. Although bulk FeCl_3 orders with a relative AB stacking between layers, the presence of a graphene layer between two layers of FeCl_3 renders the two FeCl_3 stacking configurations degenerate. This result implies that in addition to the presence of relative twist angles between intercalant layers, the layers may also undergo relative shifts in origin, as previously suggested by X-ray diffraction studies on bulk intercalant structures [23].

VI. FORMATION OF FeOCl

Finally, we observe the formation of a new monolayer that appears at the edge of the intercalated FeCl_3 monolayers in FeCl_3 -BLG when exposed to the electron beam under STEM imaging conditions with 60 kV accelerating voltage [Fig. 6(a)]. **This monolayer material is not formed during the intercalation process and is never seen at the beginning of STEM imaging.** This new monolayer forms a rectangular lattice composed of iron, chlorine, and oxygen as shown by EELS in Fig. 6(b). **Although no oxygen is present in the FeCl_3 initially, the surrounding contamination is composed of oxygen-containing hydrocarbons and iron oxide. This contamination is the likely source of oxygen for the reaction.** The constituent components and lattice shape suggest that the compound is iron oxychloride (FeOCl), a material that has previously been described in

bulk layered form [33,34]. The identification of the material is corroborated in Fig. 6(c) by an overlay of the FeOCl monolayer atomic structure, the experimental ADF image, and a STEM simulation. DFT calculations of the monolayer FeOCl electronic structure [Fig. 6(d)] indicate that the ferromagnetic and antiferromagnetic states are almost degenerate with indirect band gaps of 2.70 eV and 2.50 eV, respectively. Further exploration of the properties of this monolayer is deferred to a future paper. The creation of this novel monolayer in the FeCl_3 -intercalated bilayer system suggests the ability to engineer additional interesting materials and structures after the initial synthesis. More specifically, the microscope's electron beam is in effect used to "process" intercalants and convert them into new structures.

VII. CONCLUSIONS

In conclusion, this work demonstrates intercalation of molecules in BLG or FLG can lead to the formation of diverse complex structures. We observed the formation of crystalline FeCl_3 monolayers with a honeycomb structure like that of bulk FeCl_3 , atomically sharp boundaries between intercalated and unintercalated regions, the presence of defects, and a variety of possible orientations for the FeCl_3 relative to graphene layers. This information is useful for the study of interesting phenomena in graphene such as Klein tunneling of Dirac-like fermions, which requires atomically sharp doping boundaries, and the study of effects on the electronic band structure of graphene due to superlattice formation between the FeCl_3 and graphene honeycomb lattices [37,38]. The observation of iron interstitial defects also has possible applications in information storage due to modification of the local magnetic field by the defects. We provide evidence for coexistence of both FeCl_3 and FeCl_2 in BLG under ambient conditions, which was not observed previously and could provide a new perspective for interpreting the stability of FeCl_3 -intercalated FLG. Specifically, our results suggest that

previously reported changes in the Raman spectra of FLG-FeCl₃ might be due to the formation of FeCl₂ rather than deintercalation of FeCl₃ [11,12]. Additionally, we demonstrate the conversion of monolayer FeCl₃ into FeOCl via an electron-beam-induced reaction inside BLG, revealing intercalated BLG to be a useful vessel for creating novel 2D materials.

METHODS

A. Few-layer graphene (FLG) fabrication

The FLG was mechanically exfoliated from kish graphite onto polydimethylsiloxane (PDMS) using Scotch tape. The support grid for the FLG was prepared by milling 2 μm apertures in 50 nm silicon nitride membranes (PELCO Silicon Nitride Support Films) with a Helios Nanolab G3 CX dual beam focus ion beam – scanning electron microscope, and the FLG was then transferred to the silicon nitride membrane over the apertures using a viscoelastic stamp transfer method [39]. The BLG samples were purchased commercially (Graphene on PELCO Holey Silicon Nitride). Graphene in these samples was grown by chemical vapor deposition.

B. Vapor transport method

The vapor transport method of intercalation involves vacuum-sealing the FLG and FeCl₃ powder inside an ampule and then annealing, which causes the FeCl₃ to evaporate and spontaneously intercalate into the FLG. The ampule is prepared by sealing one end of a $\frac{1}{4}$ inch diameter borosilicate tube with a butane torch and then baking overnight at 150 $^{\circ}\text{C}$ to remove moisture. Then 0.02 g of FeCl₃ were transferred to the ampule, and the ampule was evacuated to 5 mTorr with an Edwards 5 two-stage rotary-vane vacuum pump. The ampule is attached to the vacuum setup using a quick-connect coupler. To ensure that the FeCl₃ is anhydrous, the ampule is heated to 120 $^{\circ}\text{C}$ for 30 min during evacuation and purged three times with nitrogen gas. The sample

was then inserted into the ampule, and the evacuation procedure was repeated. Once the ampule pressure gets down to 0.5 mTorr, a butane torch was used to seal the ampule approximately 10cm from the opposite end of the FeCl₃ powder. The ampule was then annealed in a Lindenburg Blue M 1-inch tube furnace to initiate the intercalation reaction. For the reaction process, the tube furnace was heated to 340 $^{\circ}\text{C}$ (measured at the center) with a ramp rate of 1 $^{\circ}\text{C}/\text{s}$ and PID setting of 20-120-30. The reaction takes place over six hours with the ampule 5cm from the center, which results in a temperature difference of ~ 15 $^{\circ}\text{C}$ between the FLG and FeCl₃ powder. Finally, the tube furnace was cooled at a rate of 1 $^{\circ}\text{C}/\text{s}$, and the intercalated sample was then removed by scoring and breaking open the ampule.

C. STEM parameters

All ADF images were acquired using an aberration-corrected Nion UltraSTEM 100TM operated at 60 kV accelerating voltage [40]. We used a semi angle convergence of 30 mrad and detection ADF semi angle range of 86-200 mrad for the intercalated FLG samples and a detection semi angle of 54-200 mrad for the intercalated BLG samples. Additionally, the length scales in our data were compared with a reference sample to ensure accuracy of the measured lengths for this work.

D. STEM simulations

STEM image simulations were performed with the QSTEM program [25]. Atomic positions were taken by laterally enlarging the DFT-optimized trilayer structures (e.g., Gr/FeCl₃/Gr with a given alignment). Images are generated using a multislice algorithm to divide the atomic potentials along the z-axis wherein each material layer is treated within its own slice and no slice contains atoms with the same xy-coordinates. The image scan resolution was set as 0.78125 \AA per pixel (with uncropped image of 192 \times 192 pixels)

and the probe array was set such that the scattering angle (432.5 mrad) was less than the detector collection angles to ensure full collection. Microscope parameters such as detector angle, voltage, defocus, aberration correction, and higher order terms were extracted from the DM3 file recorded by the microscope during experimental imaging and used to parameterize the electron beam in the simulator.

E. Resonance-Raman spectroscopy

The resonance-Raman spectra were obtained at the same spot on the intercalated sample. A tunable laser system with a dye laser (Radiant dye: 550-675 nm) and an Ar-Kr laser (Coherent Innova 70c: 450-530 nm) were used to excite the sample. The laser power was limited to 500 μ W to avoid heat-induced effects (x100 microscope objective). The light was dispersed by a T64000 Horba Jobin Yvon spectrometer equipped with 900 grooves per mm grating and a silicon charge-coupled device in single detection mode and backscattering configuration. Elastically scattered light was rejected by a long pass filter. Raman shift was calibrated on the benzonitrile reference molecule and the Raman intensity of pristine bilayer graphene to account for the wavelength dependent spectrometer sensitivity and interference with the substrate.

F. Computation Details

Spin-polarized DFT calculations used the Vienna *ab initio* Simulation Package (VASP) [41] within the Perdew-Burke-Ernzerhof (PBE) form of the generalized gradient approximation [42] along with Grimme's D2 van der Waals correction [43]. Interactions between valence and core electrons were described using the projector augmented wave method [44,45] with a plane wave basis cutoff of 400 eV. For the FeCl₃ and FeCl₂ primitive cells, the Brillouin zones were sampled with Γ -centered k-point grids of $8 \times 8 \times 1$ and $20 \times 20 \times 1$, respectively. A vacuum layer of at least 15 Å was used in all calculations and

interatomic forces were minimized to be less than 0.01 eV/Å. Spin-polarized band structure calculations for FeOCl were performed using the HSE06 hybrid functional [46,47].

ACKNOWLEDGEMENTS

This work was supported by National Science Foundation Grant DMR-1508433, Department of Energy Grant DE-FG02-09ER46554, the European Research Council Starting grant 639739, and by the McMinn and Stevenson endowment at Vanderbilt University. Supercomputer time was provided by the Extreme Science and Engineering Discovery Environment (XSEDE), which is supported by National Science Foundation Grant ACI-1053575 as well as by the Department of Defense's High-Performance Computing Modernization Program (HPCMP). Sample fabrication and characterization was conducted at the Vanderbilt Institute of Nanoscale Science and Engineering (VINSE). The STEM experiments of this research were conducted at the Center for Nanophase Materials Sciences, which is a DOE Office of Science User Facility (JCI).

The authors also wish to thank Ross Koby and Adam Cohn for assisting the fabrication of samples used in this work.

REFERENCES

-
- [1] N. Nitta, F. Wu, J. T. Lee, and G. Yushin, *Li-ion battery materials: Present and future*, Mater. Today **18**, 252 (2015).
 - [2] M. S. Dresselhaus and G. Dresselhaus, *Intercalation compounds of graphite*, Adv. Phys. **511**, 1 (2002).
 - [3] V. Etacheri, R. Marom, R. Elazari, G. Salitra, and D. Aurbach, *Challenges in the development of advanced Li-ion batteries: a review*, Energy Environ. Sci. **4**, 3243 (2011).
 - [4] J. M. Tarascon and M. Armand, *Issues and*

- challenges facing rechargeable lithium batteries*, Nature **414**, 359 (2001).
- [5] T. E. Weller, M. Ellerb, S. S. Saxena, R. P. Smith, and N. T. Skipper, *Superconductivity in the intercalated graphite compounds C6Yb and C6Ca*, Nat. Phys. **1**, 39 (2005).
- [6] J. Wan, S. D. Lacey, J. Dai, W. Bao, M. S. Fuhrer, and L. Hu, *Tuning two-dimensional nanomaterials by intercalation: materials, properties and applications*, Chem. Soc. Rev. **45**, 6742 (2016).
- [7] D. K. Bediako, M. Rezaee, H. Yoo, D. T. Larson, S. Y. F. Zhao, T. Taniguchi, K. Watanabe, T. L. Brower-thomas, E. Kaxiras, and P. Kim, *Heterointerface effects in the electrointercalation of van der Waals heterostructures*, Nature **558**, 425 (2018).
- [8] E. Pomerantseva and Y. Gogotsi, *Two-dimensional heterostructures for energy storage*, Nat. Energy **2**, 17089 (2017).
- [9] S. N. Shirodkar and E. Kaxiras, *Li intercalation at graphene / hexagonal boron nitride interfaces*, Phys. Rev. B **93**, 245438 (2016).
- [10] M. Kühne, F. Börrnert, S. Fecher, M. Ghorbani-asl, J. Biskupek, D. Samuelis, A. V Krasheninnikov, U. Kaiser, and J. H. Smet, *Reversible superdense ordering of lithium between two graphene sheets*, Nature **564**, 234 (2018).
- [11] D. J. Wehenkel, T. H. Bointon, T. Booth, P. Bøggild, M. F. Craciun, and S. Russo, *Unforeseen high temperature and humidity stability of FeCl3 intercalated few layer graphene.*, Sci. Rep. **5**, 7609 (2015).
- [12] W. Zhao, P. H. Tan, J. Liu, and A. C. Ferrari, *Intercalation of few-layer graphite flakes with FeCl3: Raman determination of Fermi level, layer by layer decoupling, and stability*, J. Am. Chem. Soc. **133**, 5941 (2011).
- [13] R. Al-Jishi, *Model for superconductivity in graphite intercalation compounds*, Phys. Rev. B **28**, 112 (1983).
- [14] R. Nandkishore, L. S. Levitov, and A. V. Chubukov, *Chiral superconductivity from repulsive interactions in doped graphene*, Nat. Phys. **8**, 158 (2012).
- [15] T. H. Bointon, I. Khrapach, R. Yakimova, A. V. Shytov, M. F. Craciun, and S. Russo, *Approaching magnetic ordering in graphene materials by FeCl3 intercalation*, Nano Lett. **14**, 1751 (2015).
- [16] B. Huang, G. Clark, D. R. Klein, D. MacNeill, E. Navarro-Moratalla, K. L. Seyler, N. Wilson, M. A. McGuire, D. H. Cobden, D. Xiao, W. Yao, P. Jarillo-Herrero, and X. Xu, *Electrical control of 2D magnetism in bilayer CrI3*, Nat. Nanotechnol. **13**, 544 (2018).
- [17] S. Jiang, J. Shan, and K. F. Mak, *Electric-field switching of two-dimensional van der Waals magnets*, Nat. Mater. **17**, 406 (2018).
- [18] B. Huang, G. Clark, E. Navarro-Moratalla, D. R. Klein, R. Cheng, K. L. Seyler, Di. Zhong, E. Schmidgall, M. A. McGuire, D. H. Cobden, W. Yao, D. Xiao, P. Jarillo-Herrero, and X. Xu, *Layer-dependent ferromagnetism in a van der Waals crystal down to the monolayer limit*, Nature **546**, 270 (2017).
- [19] K. L. Seyler, D. Zhong, D. R. Klein, S. Gao, X. Zhang, B. Huang, E. Navarro-Moratalla, L. Yang, D. H. Cobden, M. A. McGuire, W. Yao, D. Xiao, P. Jarillo-Herrero, and X. Xu, *Ligand-field helical luminescence in a 2D ferromagnetic insulator*, Nat. Phys. **14**, 277 (2018).
- [20] C. Gong, L. Li, Z. Li, H. Ji, A. Stern, Y. Xia, T. Cao, W. Bao, C. Wang, Y. Wang, Z. Q. Qiu, R. J. Cava, S. G. Louie, J. Xia, and X. Zhang, *Discovery of intrinsic ferromagnetism in two-dimensional van der Waals crystals*, Nature **546**, 265 (2017).
- [21] I. Khrapach, F. Withers, T. H. Bointon, D. K. Polyushkin, W. L. Barnes, S. Russo, and M. F. Craciun, *Novel highly conductive and transparent graphene-based conductors*, Adv. Mater. **24**, 2844 (2012).
- [22] X. Qi, J. Qu, H.-B. Zhang, D. Yang, Y. Yu,

- C. Chi, and Z.-Z. Yu, *FeCl₃ intercalated few-layer graphene for high lithium-ion storage performance*, *J. Mater. Chem. A* **3**, 15498 (2015).
- [23] J. M. Cowley and J. A. Ibers, *The structures of some ferric chloride-graphite compounds*, *Acta Crystallogr.* **9**, 421 (1956).
- [24] J. Hui, M. Burgess, J. Zhang, and J. Rodríguez-López, *Layer Number Dependence of Li+ Intercalation on Few-Layer Graphene and Electrochemical Imaging of Its Solid-Electrolyte Interphase Evolution*, *ACS Nano* **10**, 4248 (2016).
- [25] C. Koch, *Determination of Core Structure Periodicity and Point Defect Density along Dislocations*, 2002.
- [26] S. Somnath, C. R. Smith, S. V. Kalinin, M. Chi, A. Borisevich, N. Cross, G. Duscher, and S. Jesse, *Feature extraction via similarity search: application to atom finding and denoising in electron and scanning probe microscopy imaging*, *Adv. Struct. Chem. Imaging* **4**, 3 (2018).
- [27] O. S. Ovchinnikov, A. O'Hara, R. J. T. Nicholl, J. A. Hachtel, K. Bolotin, A. Lupini, S. Jesse, A. P. Baddorf, S. V. Kalinin, A. Y. Borisevich, and S. T. Pantelides, *Theory-assisted determination of nano-rippling and impurities in atomic resolution images of angle-mismatched bilayer graphene*, *2D Mater.* **5**, 041008 (2018).
- [28] J. Lee, W. Zhou, J. C. Idrobo, S. J. Pennycook, and S. T. Pantelides, *Vacancy-driven anisotropic defect distribution in the battery-cathode material LiFePO₄*, *Phys. Rev. Lett.* **107**, 085507 (2011).
- [29] G. Froehlicher and S. Berciaud, *Raman spectroscopy of electrochemically gated graphene transistors: Geometrical capacitance, electron-phonon, electron-electron, and electron-defect scattering*, *Phys. Rev. B* **91**, 205413 (2015).
- [30] M. Lazzeri and F. Mauri, *Nonadiabatic Kohn anomaly in a doped graphene monolayer*, *Phys. Rev. Lett.* **97**, 266407 (2006).
- [31] C. F. Chen, C. H. Park, B. W. Boudouris, J. Horng, B. Geng, C. Girit, A. Zettl, M. F. Crommie, R. A. Segalman, S. G. Louie, and F. Wang, *Controlling inelastic light scattering quantum pathways in graphene*, *Nature* **471**, 617 (2011).
- [32] N. Kim, K. S. Kim, N. Jung, L. Brus, and P. Kim, *Synthesis and electrical characterization of magnetic bilayer graphene intercalate*, *Nano Lett.* **11**, 860 (2011).
- [33] L. Yang, J. Deslippe, C.-H. Park, M. L. Cohen, and S. G. Louie, *Excitonic Effects on the Optical Response of Graphene and Bilayer Graphene*, *Phys. Rev. Lett.* **103**, 186802 (2009).
- [34] Y. Li and Q. Yue, *First-principles study of electronic and magnetic properties of FeCl₃-based graphite intercalation compounds*, *Phys. B Condens. Matter* **425**, 72 (2013).
- [35] M. D. Lind, *Refinement of the crystal structure of iron oxychloride*, *Acta Cryst. B* **26**, 1058 (1970).
- [36] S. R. Hwang, W.-H. Li, K. C. Lee, J. W. Lynn, and C.-G. Wu, *Spiral magnetic structure of Fe in Van der Waals gapped FeOCl and polyaniline-intercalated FeOCl*, *Phys. Rev. B* **62**, 14157 (2000).
- [37] A. F. Young and P. Kim, *Quantum interference and Klein tunnelling in graphene heterojunctions*, *Nat. Phys.* **5**, 222 (2009).
- [38] M. I. Katsnelson, K. S. Novoselov, and A. K. Geim, *Chiral tunnelling and the Klein paradox in graphene*, *Nat. Phys.* **2**, 620 (2006).
- [39] A. Castellanos-Gomez, M. Buscema, R. Molenaar, V. Singh, L. Janssen, H. S. J. Van Der Zant, and G. A. Steele, *Deterministic transfer of two-dimensional materials by all-dry viscoelastic stamping*, *2D Mater.* **1**, 1 (2014).
- [40] O. L. Krivanek, G. J. Corbin, N. Dellby, B.

- F. Elston, R. J. Keyse, M. F. Murfitt, C. S. Own, Z. S. Szilagy, and J. W. Woodruff, *An electron microscope for the aberration-corrected era*, *Ultramicroscopy* **108**, 179 (2008).
- [41] G. Kresse and J. Furthmüller, *Efficient iterative schemes for ab initio total-energy calculations using a plane-wave basis set.*, *Phys. Rev. B* **54**, 11169 (1996).
- [42] J. P. Perdew, K. Burke, and M. Ernzerhof, *Generalized Gradient Approximation Made Simple.*, *Phys. Rev. Lett.* **77**, 3865 (1996).
- [43] S. Grimme, *Semiempirical GGA-type density functional constructed with a long-range dispersion correction*, *J. Comput. Chem.* **27**, 1787 (2006).
- [44] P. E. Blöchl, *Projector augmented-wave method*, *Phys. Rev. B* **50**, 17953 (1994).
- [45] G. Kresse and D. Joubert, *From ultrasoft pseudopotentials to the projector augmented-wave method*, *Phys. Rev. B* **59**, 1758 (1999).
- [46] J. Heyd, G. E. Scuseria, and M. Ernzerhof, *Hybrid functionals based on a screened Coulomb potential*, *J. Chem. Phys.* **118**, 8207 (2003).
- [47] J. Heyd, G. E. Scuseria, and M. Ernzerhof, *Erratum: "Hybrid functionals based on a screened Coulomb potential" [J. Chem. Phys. 118, 8207 (2003)]*, *J. Chem. Phys.* **124**, 219906 (2006).

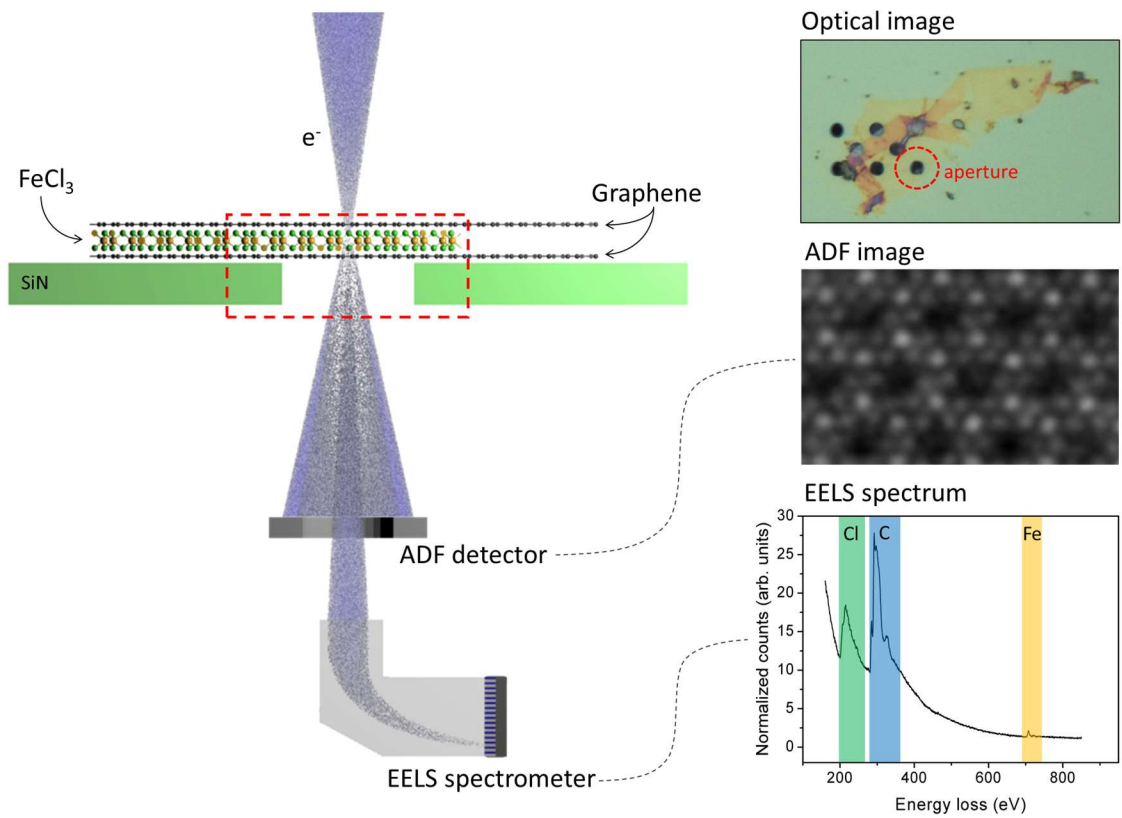


FIG. 1. (Left) Diagram of FeCl₃-BLG inside a STEM with EELS capabilities. (Top right) Optical image of the same sample with a dotted red outline showing the region where STEM is performed. (Center right) ADF image of the same sample. (Bottom right) EELS of the same sample with labels on the signals for chlorine (green), carbon (blue), and iron (yellow) atoms.

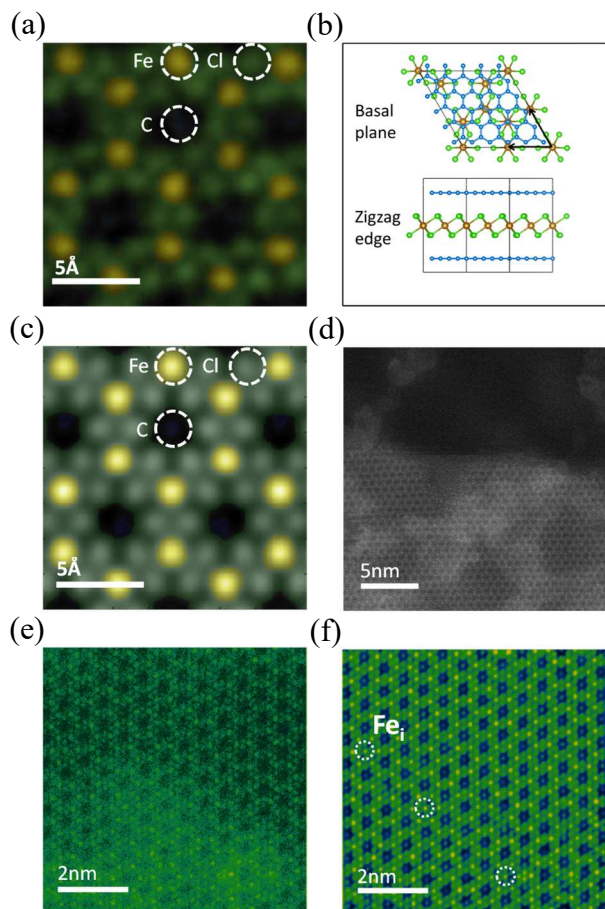


FIG. 2. (a) Colorized ADF image of FeCl_3 -BLG. (b) Diagram of FeCl_3 -BLG with black arrows displaying the primitive lattice vectors of FeCl_3 . (c) Colorized STEM simulation of FeCl_3 -BLG. (d) ADF image of intercalation boundary. (e) Unfiltered ADF image of FeCl_3 -BLG used for PCA filtering. (f) Same image as in panel (e), but filtered using components 2-10 of the PCA. Iron interstitial defects are highlighted by white dotted outlines as visible (the colors are determined by a color scale ranging from dark blue to yellow).

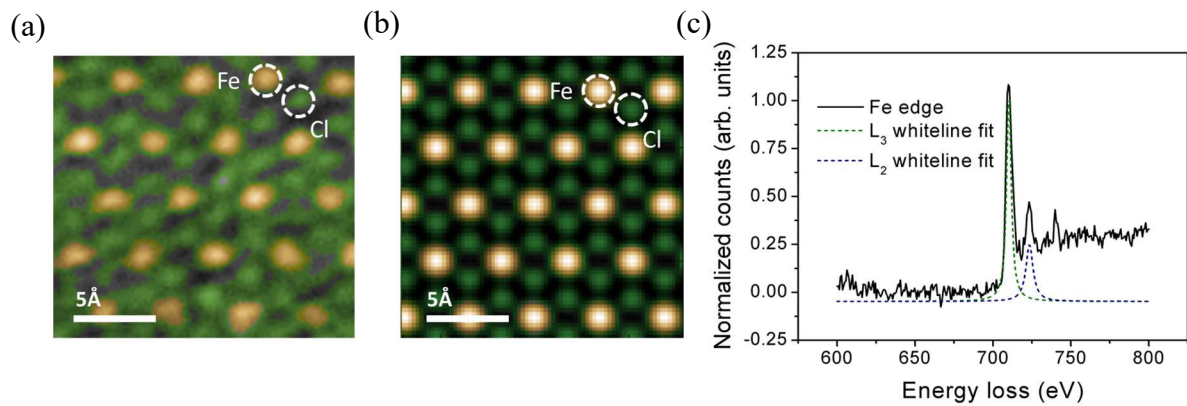


FIG. 3. Colorized (a) ADF image and (b) STEM simulation of FeCl_2 in BLG. (c) EELS spectra of the area shown in panel (a) with Lorentzian fits of the L_3 and L_2 white lines.

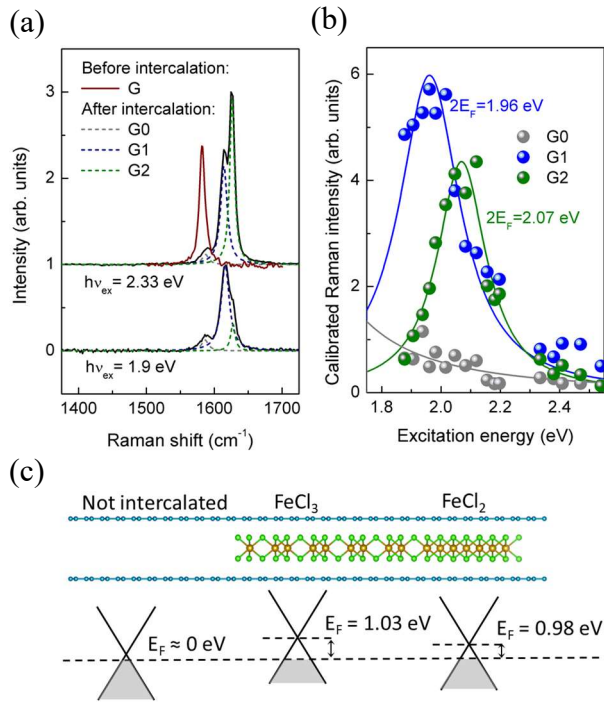


FIG. 4. (a) Raman spectra for intercalated BLG- FeCl_3 in the region of the G band with 1.9 eV (bottom) and 2.33 eV (top) excitation energies shown in black. In addition, the G band of pristine BLG before intercalation is shown in red. The dotted lines are Lorentzian fits of the G0, G1, and G2 peaks. (b) Raman intensity of the G bands as a function of excitation energy. The peak maximum is achieved when the laser energy matches twice the Fermi energy. (c) A cartoon depiction of BLG intercalated with both FeCl_3 and FeCl_2 above a diagram of the respective relative Fermi energies.

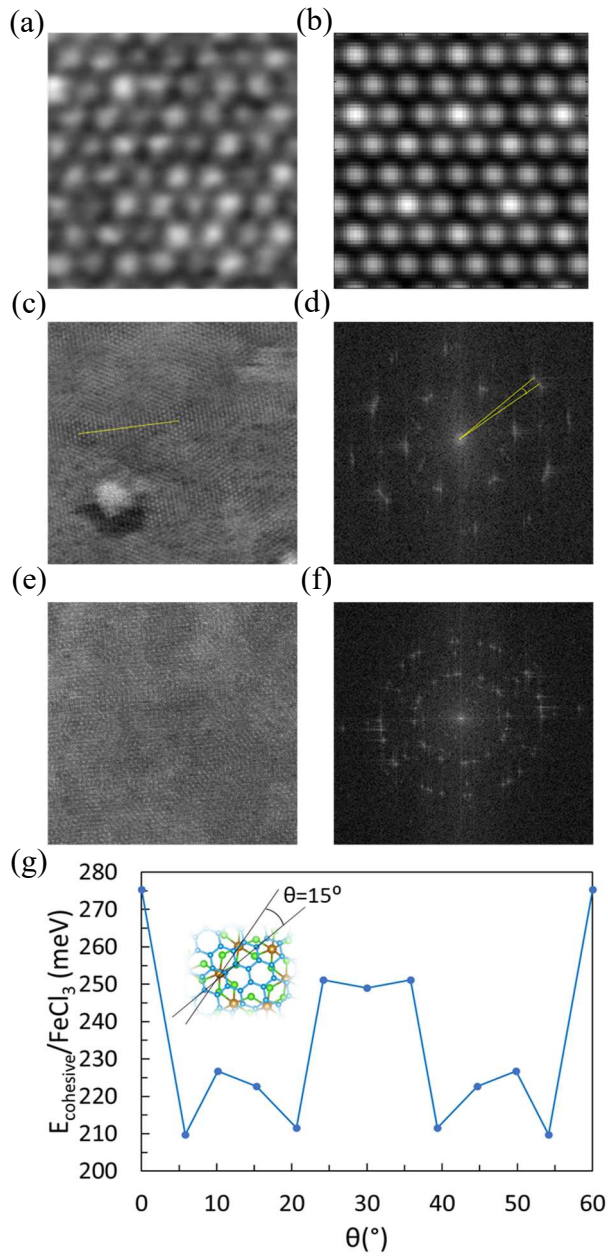


FIG. 5. (a) Annular dark-field (ADF) image of sample 1, suggested structure: ABC-stacked FeCl₃. (b) STEM simulation of ABC-stacked FeCl₃. (c) ADF image of sample 2, suggested structure: nearly aligned ABC-stacked FeCl₃. (d) Fast fourier transform (FFT) of the ADF image for sample 2. (e) ADF image of sample 3, suggested structure: FeCl₃ with uncorrelated stacking. (f) FFT of the ADF image for sample 3. (g) Cohesive energy per FeCl₃ molecule inside BLG vs. relative orientation between the crystalline axes of graphene and FeCl₃ obtained from DFT calculations, with an inset showing the angle plotted on the horizontal axis.

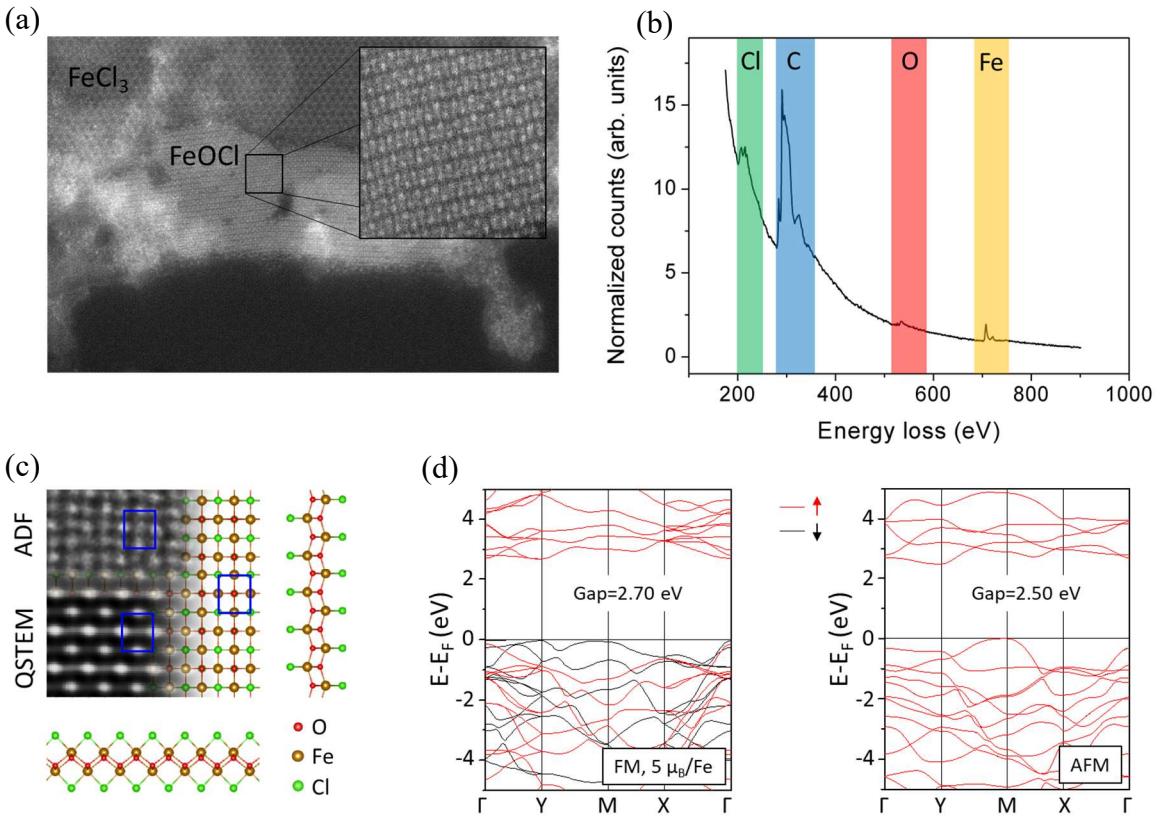


FIG. 6. (a) ADF image of the edge of the FeCl_3 monolayer after it has been irradiated during imaging. The new rectangular structure that is visible is interpreted as FeOCl . (b) EELS of the region shown in the inset of (a). (c) ADF image along with the STEM simulation of FeOCl . (d) Calculated band structure of FeOCl for ferromagnetic (left) and antiferromagnetic (right) ordering.